공학석사학위논문

전기 집진기 내부 유동 모사를 위한 다공성 매질 모델링 성능 평가

Performance of Porous Media Model for Simulating Flow Through an Electrostatic Precipitator

2023년 2월

서울대학교 대학원

기계공학부

최 웅 철

전기 집진기 내부 유동 모사를 위한 다공성 매질 모델링 성능 평가

Performance of Porous Media Model for Simulating Flow Through an Electrostatic Precipitator

지도교수 황 원 태

이 논문을 공학석사 학위논문으로 제출함

2022년 10월

서울대학교 대학원

기계공학부

최 웅 철

최 웅 철의 공학석사 학위논문을 인준함

2022년 12월

위 원 장 : 김 호 영 (인)

부위원장 : 황 원 태 (인)

위 원 : 박 형 민 (인)

Abstract

An electrostatic precipitator (ESP) collects detrimental particles of flue gas discharged from power plants. Previous studies revealed that the more even the inflow to the collection region is, the better collection efficiency is assured. However, numerous conventional investigations widely adopted porous media modeling, which has not been sufficiently validated in terms of the velocity field, not the pressure field, to resolve the flow field across the perforated plates installed within a diffuser.

Therefore, this study aims to evaluate the flow characteristics when the porous media modeling is applied to the perforated plates by conducting numerical simulation and experiment. Flow fields acquired from porous media modeling and fully resolved cases were compared to validate the model. As a result, two simulation cases showed a good agreement with the experiment at the far upstream region of the diffuser whereas the flow field across the perforated plates exhibited a quite different regime. Porous media modeling could not predict stagnated flows at the solid part of the perforated plates and wakes just beyond the plates as well as the vena contract phenomenon along the void part of the plates.

Consequently, these sorts of distortions in the flow field by porous media modeling resulted in a highly inconsistent regime compared to the one obtained from the experiment. Therefore, this modeling

needs to be largely improved to be utilized in practical prediction in the industries.

Keyword : electrostatic precipitator, flow distribution, porous media model, perforated plates, *vena contracta*
Student Number : 2021-26214

Table of Contents

List of Figures

List of Tables

Nomenclature

$\boldsymbol{u}$	Flow velocity (m/s)
M	Magnification factor
Δs	Particle displacement in a time interval
Δt	Time interval between successive images
RANS	Reynolds-average Navier-Stokes
PIV	Particle image velocimetry
ESP	Electrostatic precipitator
CCD	Charge-coupled device
CFD	Computational fluid dynamics
ROI	Region of interest
RMS	Root-mean-square
RSD	Relative standard deviation
PM	Porous media modeling
FRM	Fully resolved mesh
C_p	Pressure recovery coefficient
P_r	Reference pressure
Q	Flow rate
RZS	Recirculation zone strength
$\boldsymbol{u}$	Flow velocity (m/s)
M	Magnification factor
Δs	Particle displacement in a time interval

Δt	Time interval between successive images
RANS	Reynolds−average Navier−Stokes
PIV	Particle image velocimetry
ESP	Electrostatic precipitator
CCD	Charge−coupled device
CFD	Computational fluid dynamics
ROI	Region of interest
RMS	Root−mean−square
RSD	Relative standard deviation
PM	Porous media modeling
FRM	Fully resolved mesh
C_p	Pressure recovery coefficient
P_r	Reference pressure
Q	Flow rate
RZS	Recirculation zone strength
$\boldsymbol{u}$	Flow velocity (m/s)
M	Magnification factor
Δs	Particle displacement in a time interval

Δt	Time interval between successive images
RANS	Reynolds−average Navier−Stokes
PIV	Particle image velocimetry
ESP	Electrostatic precipitator
CCD	Charge−coupled device

CFD	Computational fluid dynamics

Chapter 1. Introduction

1.1 Study Background

An electrostatic precipitator (ESP) collects harmful particulate matter of flue gases emitted from various industries and power plants. The ESP utilizes corona discharge that forces the particulate matter to follow electrohydrodynamics (EHD). Thus, the internal flow field of the ESP has attracted considerable research interest to improve the particle collection efficiency and enhance the atmospheric air quality. Several studies utilizing EHD were conducted to assess the collection efficiency. In a pioneering study, Deutsch [1] suggested a theoretical model, after which Cooperman [2], Leonard et al. [3], Zhibin and Guoquan [4], Bai et al. [5], and Kim et al. [6] reported more advanced models for improving the ESP collection efficiency.

In the case of nonuniform flow distribution inside the ESP, the particle residence period differs considerably, and the collection efficiency is not optimal [7]. Owing to spatial limitations in real power plants, the ducts connecting each facility are curved, which generates secondary flows that deteriorate the incoming flow uniformity; consequently, the efficiency of the ESP decreases. Therefore, the ESP contains an inlet diffuser with perforated plates, which act as a gas distributor. Barratt and Kim [8] reported that the adverse pressure gradient can be altered and the fluid momentum in the boundary layer can be enhanced by installing perforated plates in the diffuser. This can improve the flow uniformity at the downstream collection plates. In addition, Sahin et al. [9–13] investigated the variations in the flow characteristics based on the porosity of these perforated plates and the separation distance between the plates. Bayazit et al. [14] reported that the pressure drop is related to the eddy formation downstream of each plate. The thickness of the perforated plate also significantly affects the pressure variations.

Because of the geometric complexity involved in the ESP flow distribution, most related studies have followed numerical approaches. Haque et al. [15–17] compared computational results with on-site test data and demonstrated consistency between the results. However, certain validation points were exceptional, and the lack of accuracy could be attributed to the use of a pitot tube, which is an invasive measurement device. Hou et al. [18] numerically studied the flow inside an ESP; they found that although the predicted pressure drop was similar to the measured data, the velocity distribution differed from real conditions. A fundamental reason for the low accuracy of the numerically predicted ESP flow distributions is that the porous media model is applied for the perforated plates within the inlet diffuser.

The porous media model was developed based on an experimental correlation established by Ergun [19] and Forchheimer [20]. It can calculate the pressure drop across a porous media using a combination of viscous resistance and inertial resistance terms expressed in terms of the mean velocity and squared mean velocity, respectively. This model is advantageous because it does not require an ultrafine mesh to resolve the exact geometry of the porous zone, which can otherwise incur exceedingly high computational costs. This model was used in conventional numerical approaches such as those adopted by Haque et al. [15–17] and Guo et al. [21] to simulate flow across perforated plates. However, it produces certain errors with respect to on-site data or experimental results.

Nield et al. [22] demonstrated that turbulent eddies of sizes comparable to that of the hole cannot exist within the voids located between the solid obstacles of a porous medium because of the strong flow suppression effect. Uth et al. [23] discovered that velocity fluctuations inside the hole are suppressed inside the porous medium and the size of turbulent eddies is bounded by the pore size. In addition, several high-fidelity computational studies [24-26] quantified the magnitude of the Reynolds stress, momentum dispersion derived from turbulent velocity fluctuations, within the porous media to determine its influence on the momentum transport occurring across the medium. The results indicated that Reynolds stress has a negligible effect on the momentum transport for small porosities, in other words, there was insignificant turbulent velocity fluctuation within pores. Thus, if the perforated plates do not have an adequately small enough porosity and hole size to suppress the velocity fluctuation and turbulent eddies, the porous media model cannot accurately predict the flow through the media. This is because the flow through high-porosity perforated plates is not substantially suppressed, while the porous media model forces the magnitude of velocity fluctuations to decrease.

In experimental studies focusing on perforated plates within an ESP, Kim [27] demonstrated that a perforated plate of porosity less than 30% generates an excessively high pressure drop, whereas a porosity greater than 50% yields an inferior flow distribution. Sahin and Ward−Smith [10, 13] visualized the flow distributions downstream of perforated plates with porosities of 40%, 50%, and 58%. Though placing a perforated plate within a diffuser helps improve flow uniformity as suggested by Barratt and Kim [8], their results showed that flow through the plate of porosity 40% had a tendency of being inclined to the wall of the diffuser, while the flow through the plate of porosity 58% experience deficient spreading effect, and being concentrated to the central region. As a result, the porosity of 40% and 58% cannot improve the flow distribution whereas the porosity of 50% succeeded to prevent flow separation. Nonetheless, the amount of reliable data for the validation of numerical approaches using porous media modeling, especially for practical perforated plates with porosities ranging from 30–60%, is insufficient.

1.2 Purpose of Research

The aim of this study was to obtain quantitative experimental data for validating computational fluid dynamics (CFD) results utilizing the porous media model for perforated plates within an ESP diffuser. In particular, we analyzed the flow for two cases: 1) porous media modeling of the perforated plates and 2) fully resolved perforated plates. The flow characteristics obtained from Reynolds−averaged Navier−Stokes (RANS)−based numerical simulations were compared with the experimental results obtained from particle image velocimetry (PIV). In addition, the flow velocity distribution and pressure drop across the diffuser with and without porous media modeling were qualitatively and quantitatively compared. Thereafter, the suitability of this modeling approach and its influence on the distribution of flow in the particle collection region were determined, which is the most essential factor for evaluating the ESP collection efficiency.

Chapter 2. Methodology

2.1. Experimental setup

An experimental 1/35 scale model of a real ESP facility is depicted in Fig. 1, which is based on the documents provided by Korea Western Power Co. The spanwise width of the collection chamber was 885 mm, and its height (including the hopper region) was 720 mm. The overall distance between the inlet and the outlet was 1895 mm, and the ducts leading into the inlet diffuser were not straight. Overall, five sets of 10 vanes were installed at various locations within the ducts to guide the flow. The two inlet diffusers were both laterally symmetric with a diffuser angle of 45° but vertically asymmetric with a 31° upper angle and 43° lower angle, as depicted in Fig. 1b. Each diffuser housed three perforated plates to create a uniform flow. In particular, the first perforated plate had a porosity of 40% for the top 70% area and a porosity of 60% for the bottom 30% area. The second plate had a uniform porosity of 50%, whereas the third plate had porosities of 50% in the central 66% area and 30% on the side surfaces. The thickness of all three plates was 3 mm. The exact location of each perforated plate is described in Section 3.3.

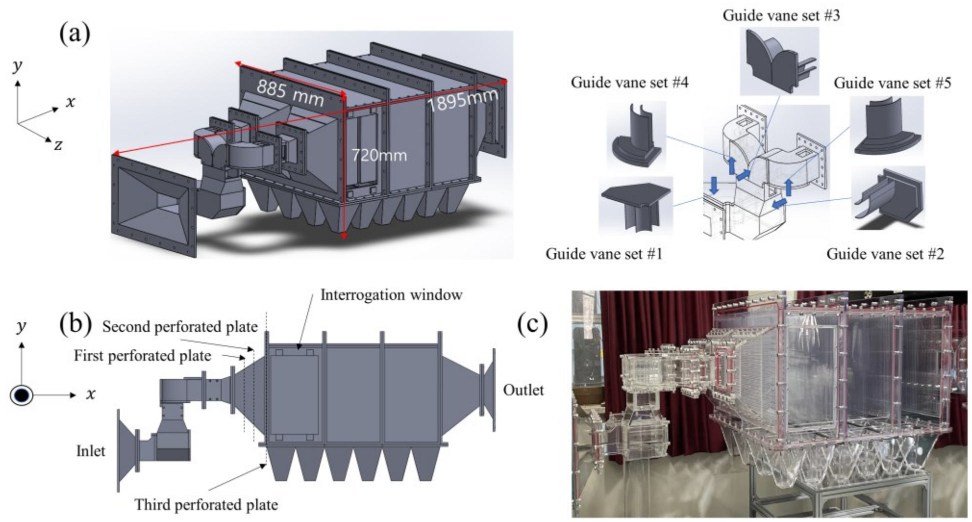

Figure 1. (a) Schematic of ESP model and inlet duct with guide vanes; (b) side view of ESP model; (c) image of model

A schematic of the experimental setup is illustrated in Fig. 2. The ESP model was connected to a closed−loop wind tunnel that provided a uniform airflow with a velocity of 0.364 m/s at the inlet of the ESP model. The Reynolds number based on the inlet hydraulic diameter of the model was 9,400. Although this Reynolds number is less than the real conditions (estimated at 10^4–10^6 according to [8], [10], [11], [15]) due to the limitations of the current wind tunnel, the measurement results can still be utilized to validate the CFD results at this intermediate condition.

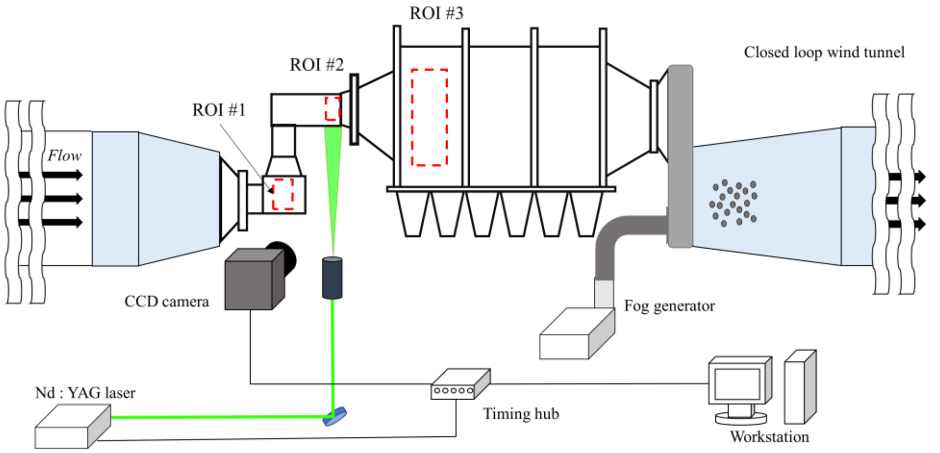

Figure 2. Schematic of the experimental setup showing ESP model connected to closed−loop wind tunnel

Table 1. PIV measurement conditions

	ROI #1 (Upstream bifurcation)	ROI #2 (Entrance to inlet diffuser)	ROI #3 (Collection chamber)
ROI size (HxV)	102 mm × 67 mm	47 mm × 76 mm	120 mm × 330 mm
PIV Δt	100 μs	50 μs	2000 μs
Camera lens	28 mm at f/4	50 mm at f/4	28 mm at f/4, 50 mm at f/4
Image pairs	1000	1000	1000

Table 2. PIV uncertainty information

	ROI #1	ROI #2	ROI #3
$\delta(M)$ (%)	3.85	1.93	1.78
$\delta(\Delta s)$ (%)	6.09	3.23	3.79
$\delta(\Delta t)$ (%)	0.03	0.06	0.002
$\delta(u_{\mathrm{PIV}})$ (%)	14.4	7.53	8.38

The 2D PIV system is depicted in Fig. 2. It comprised a double-pulsed Nd:YAG laser with 200 mJ/pulse at 532 nm. The dual-frame CCD camera contained 2048 × 2048 pixels. A fog generator seeds the tunnel with oil droplets of size ~1 μm. The images were analyzed with the open-source software PIVlab [28] which provides a recursive interrogation window reduction feature. Specifically, the initial window size was 64 px with 50% overlap, and the final pass used a 32 px window with 50% overlap. The camera exposure duration, image pair separation period Δt, and laser pulse interval were set using a timing hub, wherein Δt was adjusted based on the following three regions of interest (ROI): upstream bifurcation (ROI #1), entrance to inlet diffuser (ROI #2), and collection chamber (ROI #3). The experimental conditions are summarized in Table 1. Ensemble averages were calculated using 1000 image pairs, and erroneous vectors were corrected using a standard deviation filter. For ROI #1, one image plane was captured, and for ROI #2, five planes were measured in the lateral (i.e., out-of-plane or z-axis) direction. ROI #3 was imaged four times in the vertical (y) direction to obtain the overall flow field.

PIV velocity uncertainty was quantified from the following expression: $\boldsymbol{u}_{\mathrm{PIV}} = M\Delta s/\Delta t$, where $\boldsymbol{u}_{\mathrm{PIV}}$, M, Δs, and Δt denote the flow velocity, pixel magnification factor, particle displacement, and the time interval between successive images, respectively. To fully assess the velocity uncertainty, the uncertainty contributions of each factor need to be taken into account. The relative uncertainty of the calculated velocity can be written as follows [29-31]:

$$\delta(\boldsymbol{u}_{\mathrm{PIV}}) = 2 \times \sqrt{\delta(M)^2 + \delta(\Delta s)^2 + \delta(\Delta t)^2} \tag{1}$$

where δ denotes relative uncertainty. A coverage factor of 2 was used for a confidence level of 95%. The relative uncertainty for each factor corresponding to all ROIs is presented in Table 2.

2.2. Numerical setup and boundary conditions

The CFD simulations were conducted using ANSYS CFX 2021R2. The working fluid is air at room temperature (25 °C) to match the experiment, and is considered incompressible and at steady state. The inlet boundary condition matched the flow rate of the experiment at the inlet of the model, which corresponds to a Reynolds number of 9,400. In the CFD simulations, a completely turbulent inlet flow was assumed to ensure turbulence in the entire model, and the outlet boundary condition was set at atmospheric pressure.

Neglecting any heat transfer, each wall was treated as adiabatic. The governing equations for the steady flow are expressed as the continuity and momentum equations in Eqs. (2) and (3), respectively:

$$\nabla \cdot \boldsymbol{u} = 0, \tag{2}$$

$$(\boldsymbol{u} \cdot \nabla)\boldsymbol{u} = \nu \nabla^2 \boldsymbol{u} - \frac{1}{\rho} \nabla p, \tag{3}$$

where ρ, $\boldsymbol{u}$, p, and ν represent density, velocity, pressure, and kinematic viscosity, respectively. In this study, the Reynolds-averaged Navier–Stokes (RANS) equations were used, assuming that the fine particulate matter within the flue gas is sufficiently small that they do not affect the flow.

In prior research, various turbulence models have been utilized for examining the flow field across the perforated plates within an ESP. Wang et al. [32] used a standard k–ε model for optimizing the perforated plates for flow control and validated their CFD results using experimental results. Ye et al. [33] investigated several turbulence models to investigate the flow within an ESP and determined there were no major differences in the predictions between the standard k–ε model and the shear stress transport (SST) k–ω model. Moreover, previous studies examined the pressure loss across perforated plates using several turbulence models [33, 34], and the standard k–ε model showed the best performance. To sum up, this standard k–ε model has been widely used for simulating the flow inside an ESP [35−41], however, there has not been a sufficient review of how reliable the velocity field is for this most widely adopted turbulence model when the porous media model is applied.

Therefore, we utilized this model for evaluating flow distributions resulting from the porous media model.

For porous media modeling, the momentum source term SM, expressed in Eq. (4), is added to the RHS of the momentum equation:

$$S_M = -\frac{\mu}{\alpha}\boldsymbol{u} - \frac{\rho}{2}\zeta|\boldsymbol{u}|\boldsymbol{u}, \tag{4}$$

where α and ζ represent the permeability or viscous coefficient and the turbulent coefficient, respectively. In the turbulent regime, the first term on the RHS (i.e., viscous resistance term) is extremely small and can be neglected. Thus, the drag across the porous zone primarily includes the second term (i.e., inertial resistance term). This study considered only this inertial loss, referring to Idelchik [42]. In addition, for comparison with the porous media model, we completely resolved the perforated plates within the diffuser with an extremely fine mesh and simulated the flow to identify the variations in the flow fields within the diffuser and collection chamber.

For the simulations, the root-mean-square (RMS) convergence criterion was set at 10^{-6}. Grid independence was examined based on the pressure drop between the ESP inlet and outlet as well as the standard deviation of the spatial distribution of the streamwise velocity component (i.e., relative standard deviation, RSD) at the diffuser inlet and the front region of the collection chamber. For each case, the convergence criteria were set as a residual of less than 5%. As portrayed in Fig. 3, the fully resolved mesh requires an extremely large number of grids owing to the small hole size of the perforated plates, compared to the porous media model case. Although the porous media model required only 5.5 million grids for convergence, the fully resolved mesh required 60 million grids. Therefore, a 10× coarser grid is acceptable in the case of applying the porous media model for the perforated plates, corresponding to a significant computational benefit.

The overall pressure drop between the ESP inlet and outlet was compared for the fully resolved mesh and porous media model cases. The area-averaged pressure drop predicted with the fully resolved mesh was 37.0 Pa, and that predicted using the porous media model was 38.8 Pa. Although the porous media model utilized a less refined mesh, the discrepancy was less than 5% with respect to the fully resolved case, which is fairly consistent with the on-site Pitot tube measurement of approximately 40 Pa.

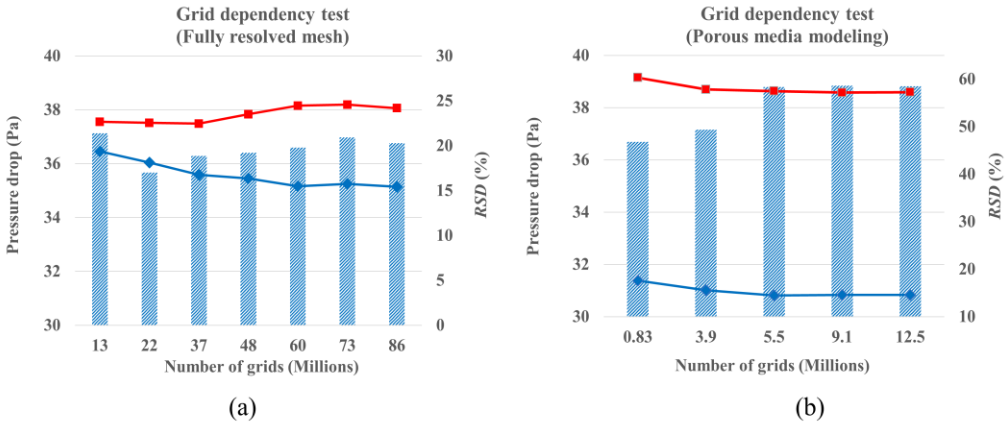

Figure 3. Grid dependency test: (a) fully resolved mesh; (b) porous media model for perforated plates.

.

Chapter 3. Results and Discussion

3.1. Bifurcation region leading into ESP

Most previous studies [15–17, 43] on ESPs investigated the flow within only one chamber out of two because of the symmetrical geometry of the ESP. Generally, flow entering the inlet diffuser is assumed as uniform. However, owing to the geometrical constraints within the power plant, several curved ducts leading up to the ESP diffuser cause the generation of complex secondary flows. Although internal guide vanes are installed to direct the flow, the occurrence of flow separation cannot be avoided. The large wake existing behind the bottom guide vane leading up to the bifurcation region is illustrated in Fig. 4. This wake causes uneven (52.4:47.6) flowrates between the left and right ducts, which creates an uneven flow distribution between the two collection chambers. Evidently, this is not desirable from the perspective of the power plant. We conducted both PIV experiments and CFD simulations to examine this flow distribution in detail.

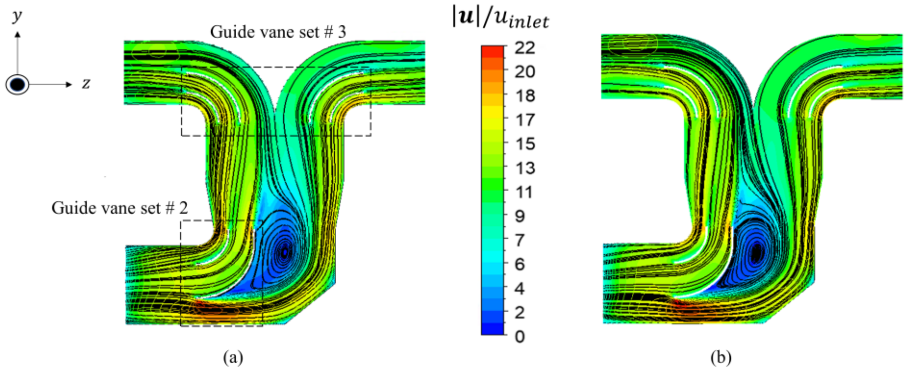

Figure 4. Streamlines and normalized velocity magnitude contour in the bifurcation region: (a) fully resolved mesh and (b) porous media modeling

As indicated in Fig. 4 (a) and (b), the streamlines and flow separation are qualitatively similar for both the fully resolved mesh and porous media modeling cases. This implies that the downstream porous media modeling of the perforated diffuser plates does not affect the upstream flow distribution. For the fully resolved mesh case, the recirculation zone defined with a negative streamwise velocity spans an area of 2.62×10^3 mm^2, whereas the PIV results indicated an area of 2.58×10^3 mm^2, i.e., an error of 1.60% between these results. Therefore, the numerical simulation is reasonably accurate in predicting the flow.

The recirculating flow field behind the bottom guide vane is examined in detail in Fig. 5. The contour of normalized streamwise velocity predicted by CFD is shown in Fig. 5(a). The streamwise velocity profiles along y/Y = 0.3 and 0.6 in Fig. 5 (b) and (c), respectively, were fairly similar between the PIV and CFD results. In addition, both the fully resolved mesh and porous media modeling cases matched the experimental results fairly well in the negative velocity region corresponding to the recirculation zone.

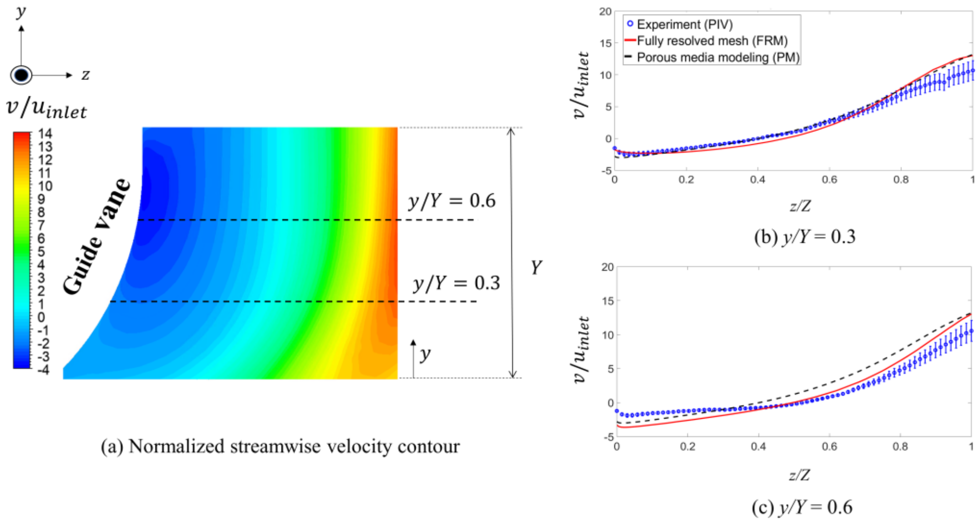

Figure 5. (a) Streamwise velocity contour behind the bottom guide vane, and comparison of streamwise velocity profiles at (b) y/Y=0.3 and (c) y/Y=0.6.

3.2. Inlet of the ESP diffuser

For the fully resolved mesh and porous media modeling cases, the flow distribution at the left and right inlets of the diffuser are presented as contours of streamwise velocity in Fig. 6. The left and right flow distributions entering the diffuser are quite nonuniform, with a flow bias toward the left and right directions, respectively. Nonetheless, the flow distributions of the fully resolved mesh and porous media modeling cases are overall similar. For quantitative analysis, *RSD* is a widely used index that describes the flow uniformity in an ESP, expressed as follows:

$$RSD\ (\%) = \frac{1}{U}\sqrt{\frac{\sum_{i=1}^{N}(u_i - U)^2}{N-1}} \times 100, \tag{5}$$

where U, u_i, and N represent the mean value, streamwise velocity component, and total number of sample data, respectively. The *RSD* of the left and right ducts predicted using the fully resolved mesh was 13.4% and 15.8%, respectively, whereas the *RSD* computed using porous media modeling was 13.9% and 15.8%, respectively. Thus, porous media modeling does not significantly influence the flow distribution upstream of the perforated plates.

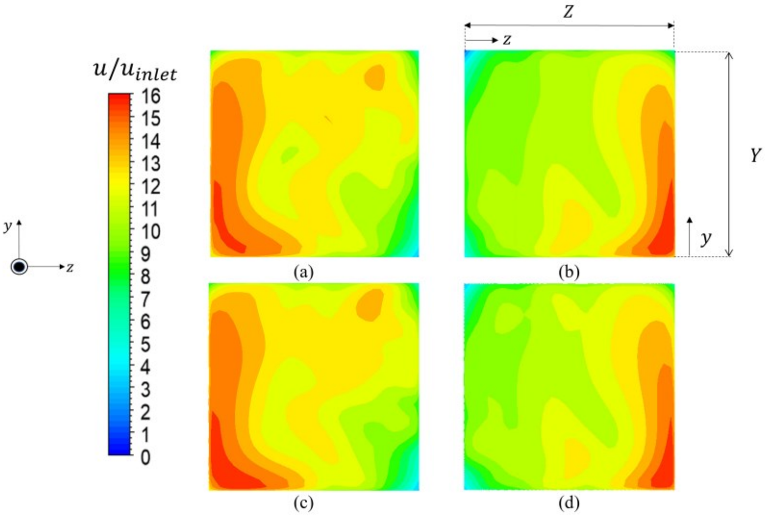

Figure 6. Contours of normalized streamwise velocity at ROI #2 (diffuser inlet) for (a) left and (b) right duct obtained from the fully resolved mesh, and (c) left and (d) right duct from porous media modeling.

The linear profiles of streamwise velocity at the diffuser inlet of the right duct for the PIV and CFD results obtained with and without porous media modeling are comparatively presented in Fig. 7. The maximum difference in mean error between the normalized velocity of the PIV and CFD based on the data presented in Table 3 is less than 7.6%. Mean error was calculated by the difference between averaged velocity measured by PIV and CFD at each location. This can be derived and propagated from the error between the real flow distribution and the CFD prediction at the flow separation region along the guide vanes installed downstream after ROI #1, where the CFD results are validated. As the *RSD* of each plane exhibits the same value, the CFD results obtained with or without the porous media modeling were consistent. As shown in Fig. 7(b) and (d), the streamwise velocity in both CFD and PIV results tends to increase at the bottom right corner. These inclined velocity distributions appear to originate from the inertial effects at the 90°-bend along the guide vanes. Furthermore, as discussed in Section 3.1 and portrayed in Fig. 6, the actual velocity distribution at the diffuser inlet is neither uniform nor parabolic. This is in contrast to previous reports in which the inlet boundary condition at the diffuser inlet exhibits uniform or parabolic profiles. Thus, this finding justifies the current research scope of observing both ducts instead of only one.

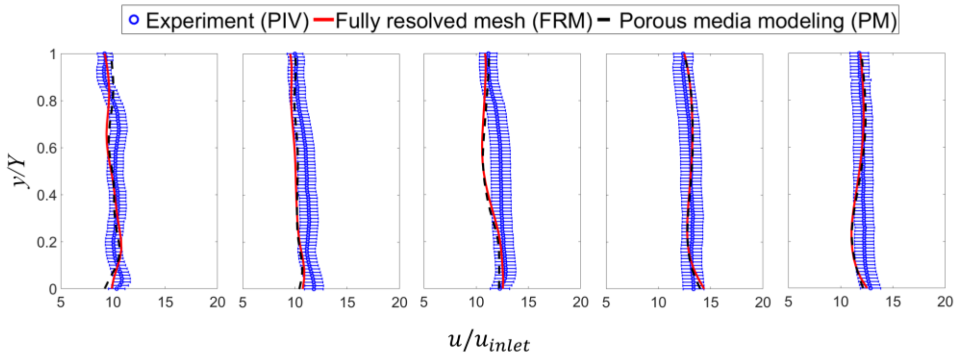

(a) $z/Z = 0.15$ (b) $z/Z = 0.26$ (c) $z/Z = 0.50$ (d) $z/Z = 0.72$ (e) $z/Z = 0.86$

Figure 7. Normalized streamwise velocity profiles in ROI #2.

Table 3. Mean error (%) between CFD results and PIV measurements

	$z/Z =$ 0.15	$z/Z =$ 0.26	$z/Z =$ 0.50	$z/Z =$ 0.72	$z/Z =$ 0.86
Fully resolved mesh	2.2	7.6	7.1	3.4	0.72
Porous media modeling	1.6	6.4	7.2	2.6	0.68

3.3. Diffuser

Gan and Riffat [44], Sahin et al. [11], and Barratt and Kim [8] analyzed the pressure losses inside the diffuser with the pressure recovery coefficient (C_p) defined as the ratio of the recovered pressure from the reference pressure to the dynamic pressure at the reference plane.

$$C_P = \frac{P - P_r}{0.5\rho \bar{u}_r{}^2}, \tag{6}$$

where P_r and $\bar{u}_r$ denote the reference pressure and the mean streamwise velocity at the reference plane, respectively. The pressure distribution within the diffuser is illustrated in Fig. 8 for the fully resolved mesh and porous media modeling cases. The diffuser inlet was set as the reference plane, and the pressure recovery coefficient was plotted along the streamwise direction. In Fig. 8(a), the 1st, 2nd, and 3rd stage perforated plates were located at x/L of 0.438 – 0.449, 0.747 – 0.760, and 0.987 – 1.00, respectively.

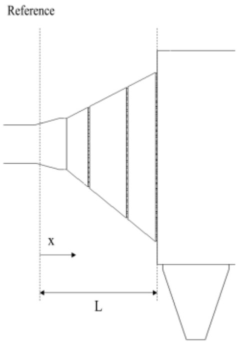

(a)

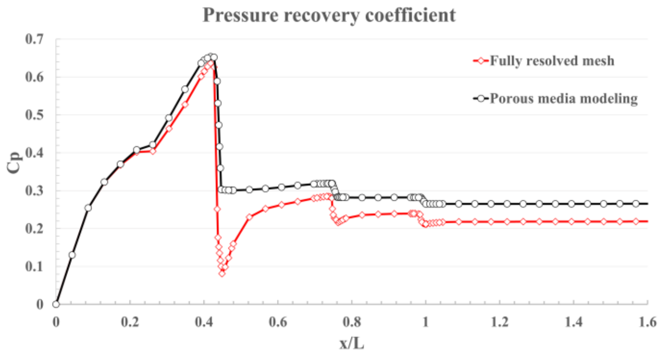

(b)

Figure 8. (a) Reference frame and
(b) pressure recovery coefficient distribution

.

At the front region of the diffuser, the C_p predicted by the fully resolved mesh and porous media modeling are quite similar up to x/L = 0.4, with a marginal increase in the deviation between the two predictions. Just before the first perforated plate, flow deflected by the solid region of the plate can be observed only with the fully resolved mesh. This results in the pressure just before the plate being slightly lower, owing to this backflow−induced recirculation zone. Shortly thereafter, C_p drops drastically for both cases as the flow passes through the first plate. The calculation with the fully resolved mesh displayed additional pressure drop until the vena contracta, caused by the jets passing through the perforations in the plate. After this point pressure recovery is observed. However, the pressure evaluated by the porous media model does not recover after the plate, but remains constant at roughly 0.3, indicating that this model cannot predict this *vena contracta* phenomenon. The overall pressure estimation also continues to be higher with the porous media model because of this deficiency in being able to accurately simulate the flow. It should be noted that Timmermans et al. [45] and Hidouri et al. [46] also demonstrated that the flow exiting a perforated plate has multiple jets with recirculation zones in between each jet. Although these overall trends were repeatedly observed for the downstream perforated plates, it is not that evident because of the relatively lower velocity at these locations.

These flow features are described in Fig. 9. It shows the side view and top view of flow streamlines according to whether a porous media model is applied. The flow field inside the hopper structures is omitted because our main interests lie in the flow across the perforated plate and the flow entering the collection chamber. As illustrated by C_p, streamlines in modeled case do not seem like rebounded or reflected by the plate. Also, the velocity field estimated with the porous media model does not have *vena contracta* across the plate. As a result, there are no jet flows at the rear of the plate. Moreover, the porous media model underestimates the generation of recirculation zones when compared to the fully resolved case.

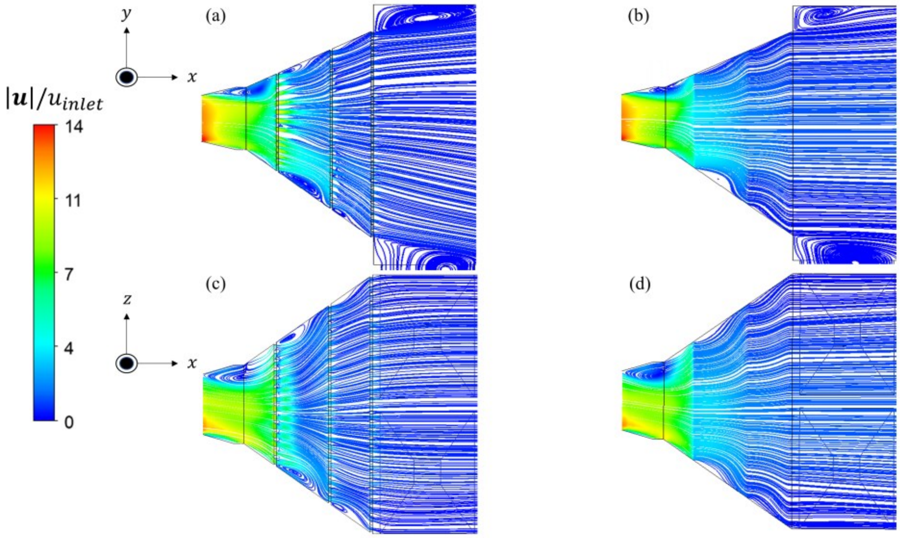

Figure 9. Side view of streamlines by (a) fully resolved mesh, (b) porous media model and Top view of streamlines by (c) fully resolved mesh and (d) porous media model

The trend of variations in *RSD* along the streamwise direction within the diffuser and collection chamber under the same reference frame is plotted in Fig. 10. The *RSD* predicted by the fully resolved mesh and porous media model were almost the same at the front region of the diffuser. However, the porous media model starts to underestimate the *RSD* value beyond $x/L > 0.2$ because it is not able to capture the backflow from the plate. The fully resolved mesh case predicted sharp leaps occurring immediately before each perforated plate, due to the velocity variations between flow stagnation regions and flow through the holes. The large distinctive peak after the plate is mainly due to the high velocity jets and reverse flow within the in-between recirculation zones, but it is also partly due to the recirculation regions located at the side surfaces of the wide-angle diffuser. The porous media model only captures these side recirculation zones, which is why the peak in *RSD* is smaller. The large nonuniformity in velocity decreases rapidly as the flow rigorously mixes before reaching the next plate for the fully resolved mesh. However, the porous media model only exhibits a fair amount of mixing after the first plate. After the second plate, the mixing is not strong which results in only a small decrease in *RSD*. After the third plate as the flow suddenly expands into the collection chamber, *RSD* slightly increases due to recirculation at the top and bottom corners, and then the flow slowly mixes downstream. The downstream flow inside the collection chamber is predicted to be more nonuniform with the porous media model than with the fully resolved mesh.

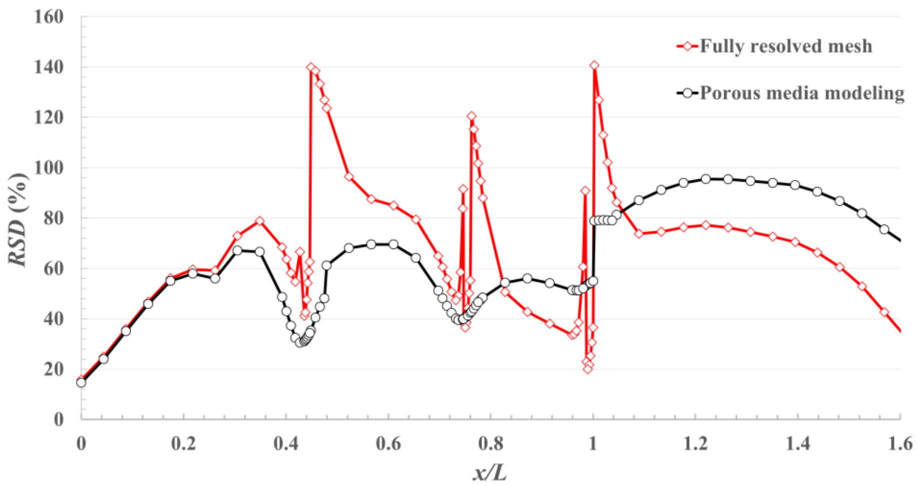

Figure 10. *RSD* distribution inside ESP.

The *RSD* distribution implies that the porous media model can contribute to the misrepresentation of flow uniformity. Thus, we adopted another quantitative flow indicator to deepen the analysis of the *RSD* variations. Zhu et al. [47] quantified a portion of the backflows in bulk flowrates, and this indicator is defined as the recirculation zone strength (*RZS*), expressed as

$$RZS = \frac{1}{Q}\int_0^A \left(\frac{\sqrt{u^2}-u}{2}\right) dA, \tag{7}$$

where Q and u represent the flow rate and streamwise velocity, respectively. If the absolute value of u is positive, the numerator of the integrand becomes zero. Otherwise, the integral value expresses the non-dimensional flowrate in the reverse direction.

The *RZS* distribution along the diffuser obtained with and without the porous media model is depicted in Fig. 11. Similar to the *RSD* and pressure recovery coefficient analysis, the *RZS* variation is consistent between the porous media model and fully resolved mesh case until x/L = 0.2. A coherent recirculation zone is generated at the wide-angle diffuser wall, centered around x/L = 0.2 – 0.3, and the backflow is reflected in the initial peak of RZS. As the flow moves through the plate, *RZS* = 0 since there is no backflow. Downstream of the first perforated plate, the fully resolved mesh predicted a drastic leap in *RZS* due to the recirculation zone between the jets, similar to *RSD*. In contrast, the porous media model only computes a small *RZS* value in between the first and second plates. Between the second and third plates backflow is not predicted for the porous media model, and it is also weak for the fully resolved mesh. After the last plate the flow enters the collection chamber, and the fully resolved mesh captures both the recirculation zones between the jets and at the top and bottom corners of the collection chamber. The porous media model only predicts the latter. Conclusively, we confirm that the porous media model does not properly capture the exact flow physics across the perforated plates.

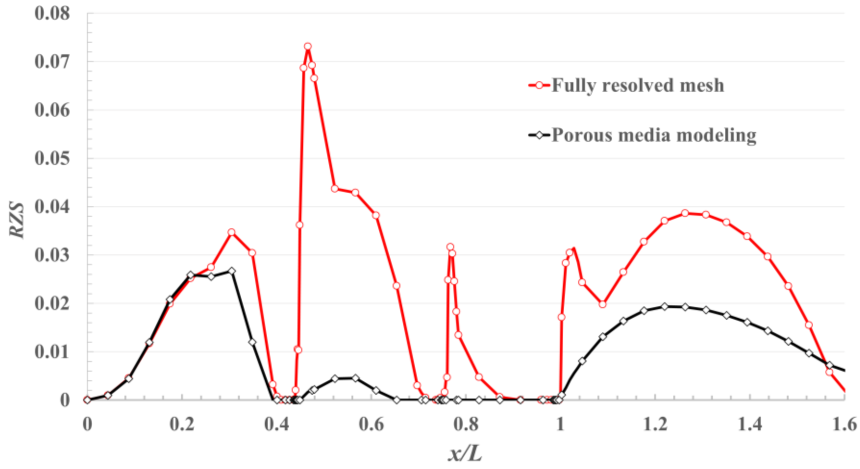

Figure 11. *RZS* distribution inside ESP.

To further understand the discrepancies in the results obtained using the porous media model and fully resolved mesh, we adopted the indices of I_1, I_2, and E suggested by Padilla [48]. I_1 is defined as

$$I_1 = \sqrt{\frac{\iint_A (u \cdot \hat{n})^2 dA}{\bar{u}^2 A}}, \tag{8}$$

where $\bar{u}$ represents an average flow velocity at the cross−section, $\hat{n}$ denotes a unit vector in a streamwise direction. I_1 quantifies the ratio of streamwise direction flowrate to bulk flowrate. The transport of fluid particles in the streamwise direction is stronger with a larger value of I_1. I_2 is defined as

$$I_2 = \sqrt{\frac{\iint_A \|u-(u \cdot \hat{n})\hat{n}\|^2 dA}{\bar{u}^2 A}}. \tag{9}$$

and it quantifies the ratio of flowrate normal to the streamwise direction to the bulk flowrate. In particular, a larger value of I_2 indicates a more active dispersion of fluid particles in the spanwise direction. Finally, E is defined as

$$E = \frac{I_2}{I_1}. \tag{10}$$

and it quantifies the strength or intensity of the spanwise behavior relative to the streamwise behavior. For larger values of E, the spanwise dispersion is more active than the streamwise transport. Using these parameters, we quantified the flow tendency in the streamwise and spanwise directions through the perforated plates. I1, I_2, and E can supplement spanwise information because RSD and RZS consider flow components only in the streamwise direction, and additionally aid in clarifying the influence of the porous media model on the flow uniformity in the collection chamber.

The calculated I_1, I_2, and E parameters are shown in Fig. 12. As illustrated in Fig. 12 (a), I_1 starts with a value of 1.0 at the diffuser inlet for both cases. Similar to the previously discussed indicators, the values of I_1 predicted by the fully resolved mesh and porous media model exhibited similar tendencies at the upstream region of the diffuser. For all three perforated plates, the porous media model computed relatively smaller jumps in the I_1 parameter compared to that of the fully resolved mesh. For I_2 in Fig. 12(b), the jumps were even smaller. Thus, stronger suppression of the spanwise component occurs with the porous media model. This results in a generally smaller value of E, as observed in Fig. 12(c), corresponding to a stronger streamwise directionality of the flow. Consequently, this causes weaker mixing in the spanwise direction within the collection chamber, which is the primary reason for the higher RSD predicted by the porous media model in Fig. 10.

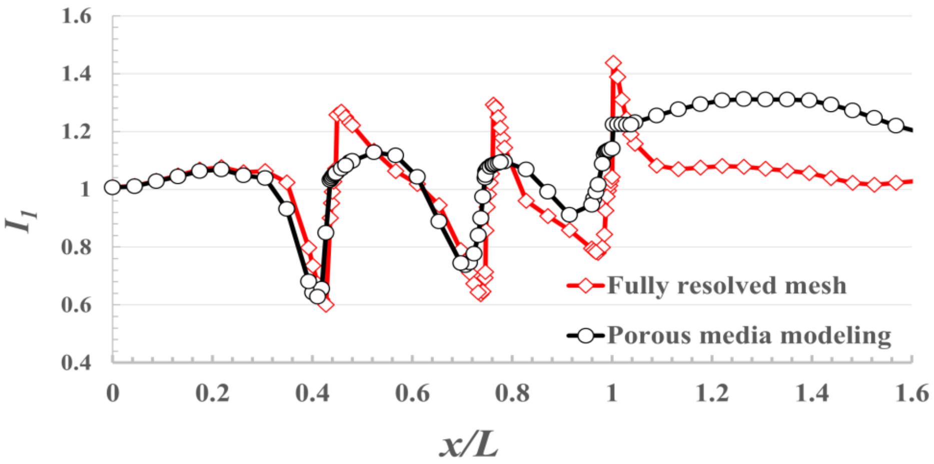

(a)

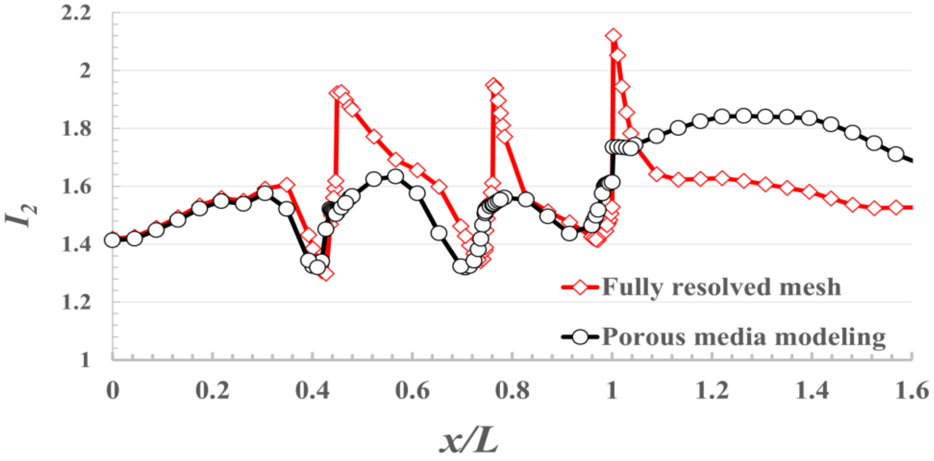

(b)

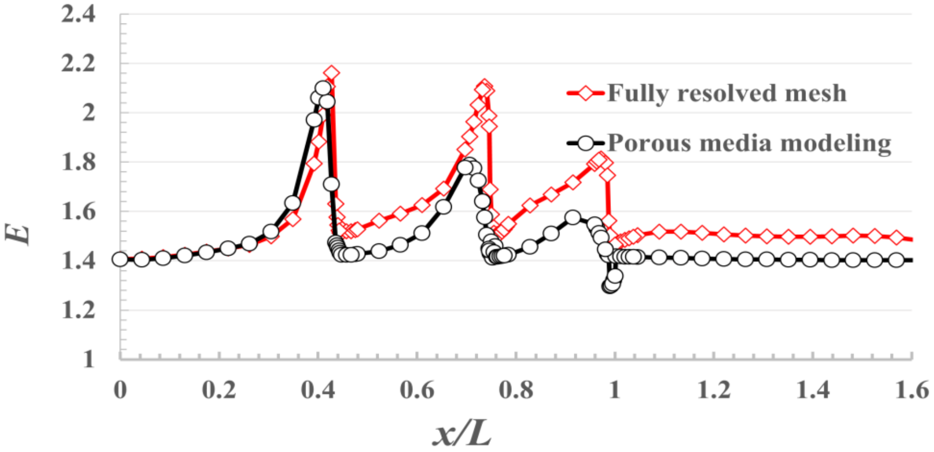

(c)

Figure 12. I_1, I_2, and E parameter distribution

3.4. Collection chamber

The contours of normalized streamwise velocity at the inlet of the collection chamber (x/L = 1.01), immediately after the last perforated plate, are presented in Fig. 13. As expected, the fully resolved mesh and porous media model predicted vastly different flow distributions. In Fig. 13 (a), the individual jets exiting the plate are clearly visible along with the in-between recirculating backflow for the fully resolved mesh. However, as depicted in Fig. 13 (b), the porous media model does not account for the holes in the plate and utilizes only the porosity information which increases the velocity magnitude in the center compared to the sides. The resulting velocity distribution is based on the model's distortion of the flow distribution upstream and downstream of the perforated plates. The top and bottom backflow regions for both cases are due to the recirculation zone caused by the step change in area of the collection chamber, as illustrated in Fig. 8 (a). The differences in flow distribution resulted in RSD of 126.9% and 79.1% at this plane for the fully resolved mesh and porous media model, respectively.

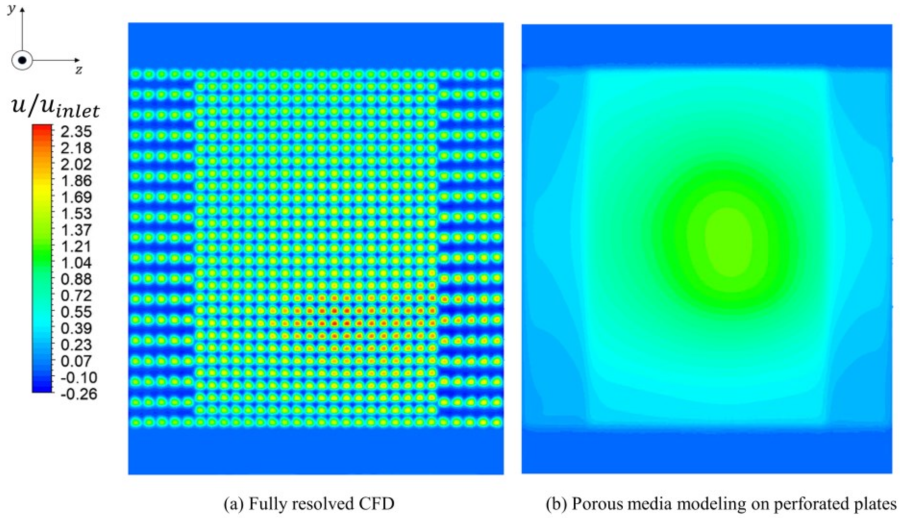

Figure 13. Normalized streamwise velocity contour at x/L = 1.01.

The streamwise velocity distributions downstream in the collection chamber at x/L = 1.6 are compared in Fig. 14. This corresponds to the ROI #3 location from Fig. 2. The individual jets have all merged and spread out for the fully resolved mesh case, resulting in an *RSD* value of 32.5%. For the porous media modeling case, the relatively strong central flow has radially spread out, creating a more conspicuous radial pattern. This results in a much higher *RSD* value of 69.5%. It should be noted that the max u/u_{inlet} has been reduced for the colorbar, compared to Fig. 13. The flow distribution clearly demonstrates the inaccurate nonuniformity predicted with porous media modeling.

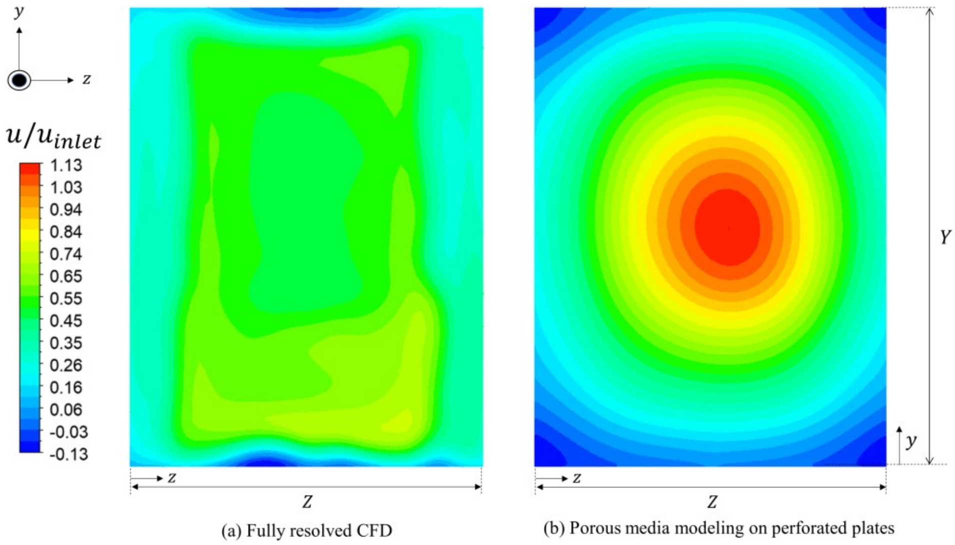

Figure 14. Contour of normalized streamwise velocity at ROI #3 (x/L = 1.6).

The qualitative flow distributions are used to obtain quantitative velocity profiles. The streamwise velocity profiles within the x/L = 1.6 plane are plotted in Fig. 15. At y/Y = 0.12 (Fig. 15a), both CFD results underestimated the velocity magnitude. The fully resolved mesh case somewhat followed the experimental trend, but the porous media model had a large discrepancy and exhibited an erroneous parabolic profile. For y/Y = 0.38, 0.64, and 0.90, the porous media model exhibited a parabolic profile again, but at these locations the streamwise velocity magnitude was mostly larger than the PIV data, while the fully resolved mesh case was a bit more similar in overall magnitude. Furthermore, in Fig. 15 (a) and (b), the velocity magnitude measured by the PIV and that predicted by the fully resolved mesh was slightly larger than that observed in Fig. 15 (c) and (d). This finding can be attributed to the geometry of the perforated plates. As mentioned before, the porosity was 40% at the top and 60% at the bottom for the 1st plate, 50% throughout for the 2nd plate, and 50% at the center and 30% on each side for the 3rd plate. Thus, the overall porosity was relatively larger near the bottom compared to the top, which resulted in a faster velocity distribution at the bottom. This is reflected in the PIV and fully resolved CFD results, whereas the porous media model failed to predict this trend. More specifically, the velocity magnitude was underestimated at the bottom (Fig. 15a) and overestimated at the top (Fig. 15b and 15c) for the porous media model. Thus, it can be seen that this model severely distorts the flow distribution within the collection chamber

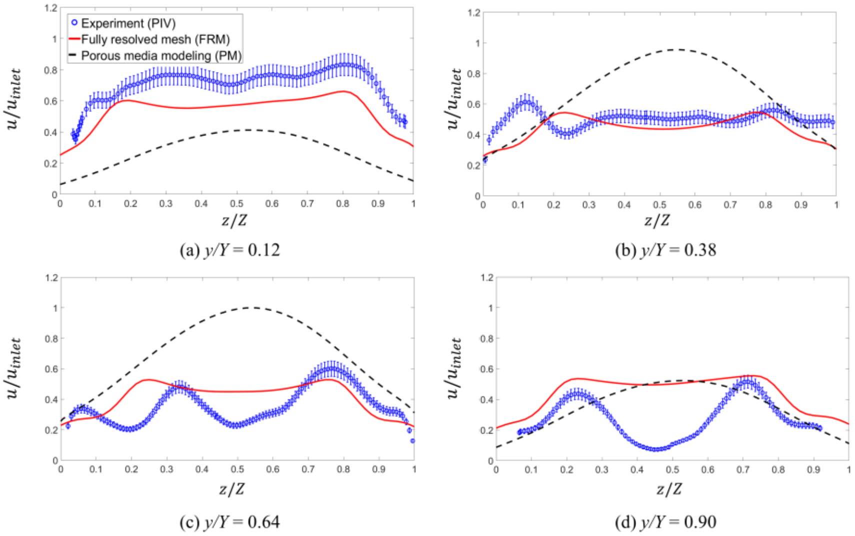

Figure 15. Normalized streamwise velocity profiles at x/L = 1.6.

The velocity field predicted using the fully resolved mesh displayed a relatively flat profile, whereas undulations were observed in the PIV results. This might be due to limitations in the standard k–ε turbulence model that was used. Compared to the results shown in Fig. 7, the skewness of flow distribution strengthened as the flow moved through the perforated plates, as shown in Fig. 15 (c) and (d). Paul et al. [49] also showed that the skewness of the velocity profile increases through a diffuser. The distortion is more severe for a skewed velocity inlet compared to a uniform inlet. They examined several turbulence models for use inside a diffuser. Overall, the RNG k–ε model exhibited the best performance compared to the standard k–ε and SST models. The standard k–ε model that we employed also displayed insufficient accuracy in capturing the skewness of the flow. Therefore, utilizing a better turbulence model should be considered for future work. Additionally, an optimization study should be performed to determine the coefficients of the standard k–ε model, similar to Li et al. [50].

Chapter 4. Conclusions

Flows through traditional porous materials such as sponges or catalysts typically employ the porous media model in CFD simulations due to the complexity in geometry. This model is also commonly used to simulate flow through perforated plates as well. However, limitations in the model do not allow for proper flow characterization across these plates. In this study, we examined the performance of the porous media model for flow entering, passing through, and exiting multiple perforated plates within a diffuser of an electrostatic precipitator (ESP) for a coal power plant. Experimental measurements with PIV and also a fully resolved CFD simulation were conducted for comparison.

The qualitative and quantitative results confirmed that the porous media model cannot accurately predict the flow distribution through perforated plates. For example, stagnation of the flow hitting the plate and the resulting backflow is not captured. Jets exiting the holes exhibit vena contracta and recirculation zones in between the jets, but this is also not observed. Furthermore, the model also overestimated the streamwise directionality of the flow. This causes weaker mixing in the spanwise direction downstream of the diffuser plates within the ESP collection chamber, resulting in a nonuniform flow distribution. This in turn will negatively affect the collection efficiency of the collection chamber.

To the best of our knowledge, this is the first detailed numerical and experimental investigation of flow characteristics across perforated plates within an asymmetric diffuser of an ESP. Although the detailed flow characteristics were markedly misinterpreted with the porous media model compared to the fully resolved simulation, the trade-off between computational cost and prediction accuracy ultimately needs to be considered.

In the future, we intend to determine the most appropriate turbulence model for predicting the flow distribution inside the collection chamber. Although the standard k–ε model has been widely employed in previous studies, its application for the ESP yields inaccurate results. Along with the turbulence model study, we are planning to investigate particle-fluid interaction with particles that have a Stokes number greater than unity. This will allow us to consider two-way coupling, which can modify the base turbulent characteristics of the flow.

Bibliography

1. Deutsch W., Bewegung und ladung der elektrizitätsträger im zylinderkondensator. Ann. Phys. 373(12) (1992) 335–344.
2. Cooperman G., A new theory of precipitator efficiency, Atmos. Environ. 5 (1971) 541–551.
3. Leonard G.L., Mitchner M., Self S.A., Experimental study of the effect of turbulent diffusion on precipitator efficiency, J. Aerosol Sci. 13 (1982) 271–284.
4. Zhibin Z., Guoquan Z., New model of electrostatic precipitation efficiency accounting for turbulent mixing, J. Aerosol Sci. 23(2) (1992) 115–121.
5. Bai B., Lu C., Chang C.L., A model to predict the system performance of an electrostatic precipitator for collecting polydisperse particles., J. Air Waste Manag. Assoc. 45: (1995) 908–916.
6. Kim S.H., Park H.S., Lee K.W., Theoretical model of electrostatic precipitator performance for collecting polydisperse particles. J. Electrostat. 50(3) (2001) 177–190.
7. Shin W,H., Hong W.S., Song D.K., Relationship between ICAC EP−7 and %RMS, Standards for Gas Flow Uniformity inside Electrostatic Precipitators, J. Korean Soc. Atmos. Environ. 26(2) (2010) 234–240.
8. Barratt D., Kim T., A banked wide−angle diffuser with application to electrostatic precipitators. Proc. Inst. Mech. Eng. Part A: J. Power Energy 229(1) (2015) 88–98.
9. Sahin B., Pressure losses in an isolated perforated plate and jets emerging from the perforated plate. Int. J. Mech. Sci. 31(1) (1989) 51–61.
10. Sahin B., Ward−Smith A.J, The use of perforated plates to control the flow emerging from a wide−angle diffuser, with application to electrostatic precipitator design. Int. J. Heat Fluid Flow 8(2) (1987) 124–131.

11. Şahin B., Ward−Smith A.J., Lane D., The pressure drop and flow characteristics of wide−angle screened diffusers of large area ratio. J. Wind Eng. Ind. Aerodynam. 58(1−2) (1995) 33–50.
12. Sahin B., Ward−Smith A.J, Effect of perforated plates on wide−angle diffuser−exit velocity profiles. J. Wind Eng. Ind. Aerodynam. 34(2) (1990) 113–125.
13. Sahin B., Ward−Smith A.J, The pressure distribution in and flow characteristics of wide−angle diffusers using perforated plates for flow control with application to electrostatic precipitators. Int. J. Mech. Sci. 35(2) (1993) 117–127.
14. Bayazit Y., Sparrow E.M., Joseph D.D., Perforated plates for fluid management: Plate geometry effects and flow regimes. Int. J. Therm. Sci. 85 (2014) 104–111.
15. Haque S.M.E., Rasul M.G., Deey A., Khan M.M.K., Zhou J., Numerical simulation of turbulent flow inside the electrostatic precipitator of a power plant. WSEAS Trans. Fluid Mech. 1(1) (2006) 96.
16. Haque S.M.E., Rasul M.G., Deey A., Khan M.M.K., Subaschandar N., Influence of the inlet velocity profiles on the prediction of velocity distribution inside an electrostatic precipitator. Exp. Therm. Fluid Sci. 33(2) (2009) 322–328.
17. Haque S.M.E., Rasul M.G., Deey A., Khan M.M.K., Subaschandar N., Flow simulation in an electrostatic precipitator of a thermal power plant. Appl. Therm. Eng. 29(10) (2009) 2037–2042.
18. Hou Q.F., Guo B.Y., Li L.F., Yu A.B., Numerical simulation of gas flow in an electrostatic precipitator. 7th Int. Conf. CFD Minerals and Process Ind. (2009).
19. Ergun S., Fluid flow through packed columns. Chem. Eng. Prog. 48 (1952) 89–94.
20. Forchheimer P., Wasserbewegung durch boden. Z. Ver. Deutsch. Ing. 45 (1901) 1782–1788.
21. Guo B.Y., Hou Q.F., Yu A.B., Li L.F., Guo J., Numerical modelling of the gas flow through perforated plates. Chem. Eng. Res. Des. 91(3) (2013) 403–408.

22. Nield D.A., The limitations of the Brinkman–Forchheimer equation in modeling flow in a saturated porous medium and at an interface. Int. J. Heat Fluid Flow 12(3) (1991) 269–272.
23. Uth M.F., Jin Y., Kuznetsov A.V., Herwig H., A direct numerical simulation study on the possibility of macroscopic turbulence in porous media: Effects of different solid matrix geometries, solid boundaries, and two porosity scales.Phys. Fluids 28(6) (2016) 065101.
24. Chandesris M., d'Hueppe A., Mathieu B., Jamet D., Goveau B., , Direct numerical simulation of turbulent heat transfer in a fluid–porous domain. Phys. Fluids 25(12) (2013) 125110.
25. Jin Y., Kuznetsov A,V., Turbulence modeling for flows in wall bounded porous media: an analysis based on direct numerical simulations. Phys. Fluids 29(4) (2017) 045102.
26. Jouybari N.F., Lundström T.S., Investigation of post–Darcy flow in thin porous media. Transp. Porous Media 138(1) (2021) 157–184.
27. Kim D.U., Jung S.H., Kim J.T., Lee S.S., Flow distribution in an electrostatic precipitator with a perforated plate. Clean Technol. 25(2) (2019) 147–152.
28. Thielicke W., Sonntag R., Particle image velocimetry for MATLAB: Accuracy and enhanced algorithms in PIVlab. J. Open Res. Soft. 9(1) (2021) 12.
29. Sciacchitano A., Uncertainty quantification in particle image velocimetry. Meas. Sci. Technol. 30 (9) 092001 (2019).
30. Lawson N.J., Rudman M., Guerra A., Liow J.–L., Experimental and numerical comparisons of the break–up of a large bubble. Exp. Fluids 26 (1999) 524–534.
31. Choi D., Park H., Flow–structure interaction of a starting jet through a flexible circular zone. J. Fluid. Mech. 949, A39 (2022).
32. Wang P., Pan W., Dai G., A CFD–based design scheme for the perforated distributor with the control of radial flow. AIChE J. 66 (5) (2020).
33. Ye X.L., Su Y.B., Guo B.Y., Yu A.B., Multiscale simulation of

the gas flow through electrostatic precipitators. Appl. Math. Model. 40(21−22) (2016) 9514–9526.
34. Barros Filho J.A., Santos A.A., Navarro M.A., Jordao E., Effect of chamfer geometry on the pressure drop of perforated plates within thin orifices. Nucl Eng & Des. 284 (2015) 74−79.
35. La Rosa D.M., Rossi M.M.A., Ferrarese G., Mlalvasi S., On the pressure losses through multistage perforated plates. ASME. J. Fluids Eng. 143 (6) (2021) 061205
36. Nikas K,S.P., Varonos A.A., Bergeles G.C., Numerical simulation of the flow and the collection mechanisms inside a laboratory scale electrostatic precipitator. J. Electrostat. 63(5) (2005) 423–443.
37. Adamiak K., Numerical models in simulating wire−plate electrostatic precipitators: A review. J. Electrostat. 71(4) (2013) 673–680.
38. Kallio G.A., Stock D.E., Interaction of electrostatic and fluid dynamic fields in wire—plate electrostatic precipitators. J. Fluid Mech. 240 (1992) 133–166.
39. Varonos A.A., Anagnostopoulos J.S., Bergeles G.C., Prediction of the cleaning efficiency of an electrostatic precipitator. J. Electrostat. 55(2) (2002) 111–133.
40. Zhang X., Wang L., Zhu K., Particle tracking and particle−wall collision in a wire−plate electrostatic precipitator. J. Electrostat. 63(11) (2005) 1057–1071.
41. Talaie M.R., Mathematical modeling of wire−duct single−stage electrostatic precipitators. J. Hazard. Mater. 124(1−3) (2005) 44–52.
42, Idelchik I.E., Steinberg O., Handbook of hydraulic resistance. Begell House Inc., Redding, 2007.
43. Guo B.Y., Yang S.Y., Xing M., Dong K.J., Yu A.B., Guo J., , Toward the development of an integrated multiscale model for electrostatic precipitation. J. Ind. Eng. Chem. 52(33) (2013) 11282–11293.
44. Gan G., Riffat S.B., Pressure loss characteristics of orifice

and perforated plates. Exp. Therm. Fluid Sci. 14(2) (1997) 160–165.

45. J. Timmermans, M. Vanierschot, E. Van den Bulck, Flow instabilities in the near wake of a perforated plate. 9th Nat. Cong. Theor. Appl. Mech., Brussels, 2012.

46. A. Hidouri, N. Yahya, T. Boushaki, A. Sadiki, J.C. Sautet, Numerical and experimental investigation of turbulent three separated jets. Appl. Therm. Eng. 104 (2016) 153–161. https://doi.org/10.1016/j.applthermaleng.2016.05.021

47. Zhu X., Li R., Li D., Zhang P., Qian R., Experimental study and RANS calculation on velocity and temperature of a kerosene-fueled swirl laboratory combustor with and without centerbody air injection. Int. J. Heat Mass Transfer 89 (2015) 964–976.

48. Padilla A., The effect of upstream perturbations on 3D annular diffusers, Ph.D. Dissertation, Stanford University, 2012.

49. Paul A.R., Ranjan P., Patel V.K., Jain A., Comparative studies on flow control in rectangular S-duct diffuser using submerged-vortex generators.Aerosp. Sci. Technol. 28(1) (2013) 332–343.

50. Li D., Zhang F., Long J., Luo D., The numerical simulation of a rectifying device with a perforated plate. Flow Measure. Instrument. 38 (201) 27–35.

초 록

전기집진기는 발전소에서 발생하는 배기 가스에 존재하는 유해 미세 입자를 여과하여 대기 중 미세 먼지를 저감하는 기능을 한다. 수많은 선행 연구들에 따르면 전기 집진기의 집진 성능 향상을 위해서는 집진 영역으로 들어가는 유동장이 균일할수록 좋다. 그러나 대부분의 선행 연구는 디퓨저 내부 타공판을 통과하는 유동에 대해 porous media modeling을 적용하는 경우가 많았는 데, 압력장과 달리 속도장 측면에서 이 모델링의 적합성은 충분히 검증되지 않았다.

따라서 본 연구는 전기집진기 내부 유동에 대한 porous media model의 적절성을 평가하기 위해 전산 시뮬레이션과 실험을 수행하였다. Porous media model을 적용하여 계산한 유동장과 실질적인 타공판의 형상을 반영하여 계산한 유동장을 비교하였다. 이 두 가지 경우로부터 얻은 유동장은 디퓨저 상류에서는 실험 결과와 일치하는 경향을 보였으나, 디퓨저 내부에 설치된 타공판 전후 유동장에서는 모델링 적용 여부에 따라 매우 큰 차이를 보였다. 전반적으로, 이 모델은 타공판의 고체 영역에서 발생한 정체 유동 및 타공판 후방에서 발생하는 후류를 반영하지 못 하는 특징을 보였고, 유동이 타공판의 빈 공간을 통과하면서 유동의 단면이 감소하여 발생하는 베나 콘트랙타 현상을 예측하지 못 한다는 점이 발견되었다.

결과적으로, 이와 같은 유동장의 왜곡은 집진 영역으로 들어가는 유동을 실험과 매우 다르게 해석하였다. 따라서 이와 같은 porous media model은 전기집진기 내부 유동장 해석과 같은 산업계에서의 광범위한 활용을 위해서는 추가적인 개선이 필요하다.

주요어 : 전기집진기, 유동 분포, porous media model, 타공판

학번 : 2021-26214